Anisotropies and Universality of Buoyancy-Dominated Turbulent Fluctuations: A Large-Eddy Simulation Study

MARTA ANTONELLI

Dipartimento di Fisica, University of Genoa, Genoa, Italy

ALESSANDRA LANOTTE

CNR-ISAC, and Istituto Nazionale di Fisica Nucleare, Lecce, Italy

ANDREA MAZZINO

Dipartimento di Fisica, University of Genoa, Consorzio Nazionale Interuniversario per le Scienze Fisiche della Materia, and Istituto Nazionale di Fisica Nucleare, Genoa, Italy

(Manuscript received 25 July 2006, in final form 10 October 2006)

ABSTRACT

Turbulent fluctuations of both velocity and temperature fields, issuing from high-resolution large-eddy simulations, have been analyzed in convective boundary layers. The numerically simulated flows are strongly anisotropic at large scales: this is due both to the action of buoyancy and to the imposed geostrophic wind. Their relative weight is varied so that one experiment's results are much more convective than the other. To properly disentangle anisotropic properties, the authors exploit both standard statistical indicators, like skewness coefficients, and the three-dimensional rotational group decomposition SO(3). Two main conclusions can be drawn. First, despite the strong anisotropies at large scales, isotropy is statistically recovered at scales much smaller than the large ones. Second, relevant statistical indicators of turbulence such as the scaling exponents, of both velocity and temperature fields, are remarkably close for the two experiments. Implications of these findings for the problem of subgrid-scale modeling are discussed.

1. Introduction

The concept of spatiotemporal fluctuation is probably the best way to characterize turbulent atmospheric systems. Such fluctuations are triggered by external features like boundaries, imposed mean flows or large-scale gradients. Physical driving mechanisms, in natural phenomena or in laboratory experiments, often generate large-scale turbulent fluctuations that are strongly anisotropic and highly nonuniversal. The latter property reflects the enormous variety of external features able to generate turbulent flows.

In spite of this complexity, turbulent fluctuations, at scales much smaller than those at which turbulence is created, are believed to be statistically isotropic and, to a certain degree, universal. In particular, scaling exponents characterizing statistical objects are believed to be universal, that is, almost independent of the details of large-scale mechanisms driving turbulent fluctuations. This is the framework of the well-known Kolmogorov (1941) theory of turbulence [see, e.g., Frisch (1995) for a modern presentation]. To which extent turbulent fluctuations share the universality and isotropy properties has been a central matter of research for the last 10 years (see, e.g., Sreenivasan and Antonia 1997; Shraiman and Siggia 2000; Falkovich et al. 2001; Mininni et al. 2006). Understanding the above aspects has relevant consequences in applications related, for example, to the small-scale subgrid (SGS) parameterizations adopted in large-eddy simulations (LES). Indeed, modern approaches to closure problems commonly use isotropic scaling exponents as the basic ingredients to build subgrid-scale models. The best examples are the fractal (Scotti and Meneveau 1997) and multifractal (Basu et al. 2004) interpolation schemes. When applying these closures to realistic coarse-grained models of turbulence, both the universality and isotropy recovery issues are of primary importance. Furthermore, the

Corresponding author address: Alessandra S. Lanotte, CNR-ISAC, Str. Lecce-Monteroni, 73100 Lecce, Italy.
E-mail: a.lanotte@isac.cnr.it

DOI: 10.1175/JAS3951.1

eddy-viscosity concept at the base of many SGS models is intrinsically isotropic, thus supposing that anisotropic fluctuations vanish at the filter scale. Thus the question arises if anisotropic fluctuations are sufficiently weak at the cutoff scale that we can condense their importance in terms of simple coefficients, or eventually neglect them.

Let us be more precise and briefly anticipate some of the results discussed at length in the sequel. We define the potential temperature structure functions as $S^{(p,\theta)}(\mathbf{x}, \mathbf{r}) \equiv \langle [\theta(\mathbf{x} + \mathbf{r}) - \theta(\mathbf{x})]^p \rangle$, and the velocity longitudinal structure functions as $S^{(p,u)}(\mathbf{x}, \mathbf{r}) \equiv \langle \{[\mathbf{u}(\mathbf{x} + \mathbf{r}) - \mathbf{u}(\mathbf{x})] \cdot \hat{\mathbf{r}}\}^p \rangle$. These are moments of temperature or velocity increments measured over a distance $\mathbf{r}$. At this stage, for simplicity, we can refer to them by using $S^{(p)}(\mathbf{x}, \mathbf{r})$, where the field under investigation can be either the temperature or the velocity. For a very large Reynolds number and in a range of scales r well separated from the injection and the dissipative scales, in the so-called inertial range, the structure functions $S^{(p)}(\mathbf{x}, \mathbf{r})$ are expected to behave as power laws. This is the essential assumption of any phenomenological turbulence theory à la Kolmogorov (1941). The simplest situation is that of a homogeneous and isotropic system, where

$$S^{(p)}(\mathbf{x}, \mathbf{r}) \equiv S^{(p)}(r) \propto c_0 r^{\xi_p^{(\mathrm{iso})}}, \tag{1}$$

c_0 being a constant that depends on the details of the large-scale forcing mechanisms. Independently of the mean flow or mean temperature profile, the exponents $\xi_p^{(\mathrm{iso})}$ fully characterize the statistical behavior of turbulent fluctuations in the inertial range. They are also the basic ingredients of the multifractal interpolation schemes (Basu et al. 2004) and the associated SGS modeling.

The important question we address in the present paper concerns the modification (if any) of the turbulent statistics and in particular of the scaling properties (1), focusing on the role of anisotropy, while leaving aside the effects due to inhomogeneity. The interplay between inhomogeneities and anisotropies is a further source of difficulties and its investigation will be left for future studies.

The presence of anisotropy clearly induces a dependence on the direction $\mathbf{r}$, and any statistical observable need to be properly defined. A very simple way to proceed, avoiding technicalities, is to think of the generic structure function $S^{(p)}(\mathbf{r})$ as decomposed into different contributions due to the isotropic and anisotropic fluctuations:

$$S^{(p)}(\mathbf{r}) = c_0 r^{\xi_p^{(\mathrm{iso})}} + c_1 r^{\xi_p^{(\mathrm{aniso1})}} + \cdots, \tag{2}$$

where the first term is the isotropic contribution to the structure function, the second term is the first of the anisotropic contributions, and so on. In (2), c_1 is a constant too. Details on this expansion will be given in section 5. Even if the expression (2) is very crude, it is clear that if the anisotropic contributions are comparatively negligible with respect to the isotropic one, we can say that isotropy is statistically restored in the inertial range [see Biferale and Procaccia (2005) for a complete review of anisotropic turbulence and references therein]. On the contrary, if these terms happen to be of the same order or larger than the isotropic term, that is, $A(r) \equiv c_1 r^{\xi_p^{(\mathrm{aniso1})}} / c_0 r^{\xi_p^{(\mathrm{iso})}} \gg 1$, then the inertial range statistics would be anisotropic at any scale, a fact that we could not neglect when deriving models and closures. It is also clear the relevance of this issue for the SGS modeling. Indeed, if isotropy was statistically restored then the classical multifractal interpolation schemes (Basu et al. 2004) should be applicable to construct SGS models. On the contrary, a new strategy able to incorporate anisotropic corrections should be implemented.

Let us assume that isotropy is restored in some range of scales: we conventionally refer to these as inertial range scales to distinguish them from the large ones where turbulence is generated, and from those affected by the SGS closures. A related question is that of the possible dependence of the (leading) isotropic scaling exponents appearing in (2) on the degree of convection. This is the universality problem, here in terms of the different degree of convection, crucial to understand how much some statistical properties, as for example the scaling exponents, are representative of different turbulent systems (Sreenivasan and Antonia 1997). In terms of SGS parameterizations, this amounts to understanding whether or not a given multifractal interpolation scheme is universal and thus valid for different experimental conditions.

The main aim of the present paper is to contribute to the understanding of both questions, that is, the characterization of the turbulent statistics in an anisotropic situation and its dependence on the imposed degree of convection.

To do so, we consider two LES studies of the planetary boundary layer (PBL), characterized by different degrees of convection. In both situations, the system is strongly anisotropic because of the combined effects of the buoyancy force and of the shear. We analyze the statistics of the velocity and temperature fields, first considering the behavior of classical statistical observables such as the skewness factor and the probability density functions (PDFs) of turbulent fluctuations measured along different spatial directions. While giving qualitative indications on the properties of the systems,

this analysis is not sufficient when considering the isotropy and the universality issues. A new statistical tool borrowed from the theoretical physics domain is then introduced: it is three-dimensional rotational group decomposition, which can properly disentangle the isotropic from the anisotropic turbulent fluctuations (Arad et al. 1999a). Previously, it has been fruitfully applied to study anisotropic systems in analytical, numerical, and experimental works (Arad et al. 1999b; Biferale and Procaccia 2005). Recently, Hofbauer et al. (2005) have used the SO(3) decomposition to test the performances of a variety of SGS models, and check how these reproduce the isotropic and anisotropic fluctuations of the turbulent velocity field.

Thanks to the application of the SO(3) decomposition, new information can be extracted about the turbulent fluctuations in PBLs also. The results that we obtained clearly point in favor of the isotropy restoration within the mixed layer. On the other hand, as we will see, things are not as conclusive about the universality of inertial range turbulence statistics, that is, its independence of the conditions at large scales.

The paper is organized as follows: section 2 is devoted to reviewing the large-eddy simulation strategy. In section 3, we present the numerical studies, while in section 4 we show some results in terms of what we called classical observables. In section 5, the SO(3) decomposition is introduced and applied to the LES data. Sensitivity tests comparing experiments at two different resolutions are described in section 6. Final remarks are left to section 7.

2. The large-eddy simulation model

The PBL dynamics are described, in our model, in terms of the Navier–Stokes equations coupled, via the Boussinesq term, with the evolution equation of the potential temperature $\theta(x)$. The huge range of spatial and time scales involved makes the direct numerical simulation a very difficult task. In a large-eddy simulation, only the motion associated with the largest turbulent eddies is explicitly solved, while the small-scale dynamics, partly belonging to the inertial range of scales, is described in a statistical consistent way. In other words, small-scale dynamics is parameterized in terms of the resolved, large-scale velocity and temperature fields.

This is done applying a low-pass filter to the governing equations for the velocity and potential temperature. As an example, such a filter applied to the ith component of the velocity field, u_i, ($u_1 = u$, $u_2 = v$, $u_3 = w$), is defined by the convolution:

$$\overline{u}_i(\mathbf{x}) = \int u_i(\mathbf{x}')G(\mathbf{x} - \mathbf{x}')\, d\mathbf{x}', \tag{3}$$

TABLE 1. Physical parameters of the two simulated CBLs. Here, L_x, L_y, and L_z account for the domain extension; $\Delta x = L_x/NX$, $\Delta y = L_y/NY$, and $\Delta z = L_z/NZ$ are the grid mesh spacings in the x, y, and z coordinates; $Q*$ is the heat flux from the bottom boundary; U_g is the geostrophic wind; z_0 is the roughness length; z_i is the mixed layer depth; L_{mo} is the Monin–Obukhov length; $w*$ is the convective velocity scale: $w* \equiv [(g/\theta)Q*z_i]^{1/3}$ where g/θ_0 is the buoyancy term and θ_0 is a reference temperature; $u*$ is the friction velocity; $\tau* \equiv z_i/w*$ is the large-scale eddy turnover time; T is the total simulation time, after the quasi steady state was reached; t_{samp} is the sampling time for the velocity and temperature field Eulerian configurations; λ is the estimated Taylor scale; and Re_λ is the estimated Taylor scale-based Reynolds number.

Parameters	Units	Expt 1	Expt 2
L_x, L_y	(km)	12	12
L_z	(km)	2.5	2.5
Δx, Δy	(m)	~47	~47
Δz	(m)	~10	~10
$Q*$	(m K s^{-1})	0.24	0.24
U_g	(m s^{-1})	18.0	3.6
z_0	(m)	0.16	0.16
z_i	(m)	1800	1850
L_{mo}	(m)	−340	−11
$-z_i/L_{\mathrm{mo}}$		5.3	164
$w*$	(m s^{-1})	2.4	2.4
$u*$	(m s^{-1})	1.0	0.3
$\tau*$	(s)	750	770
T	(s)	~20$\tau*$	~20$T\tau*$
λ	(cm)	29	29
Re_λ		28 000	23 000

where $\overline{u}_i(\mathbf{x})$ is the filtered field and $G(\mathbf{x})$ is a three-dimensional filter function. As in Moeng (1984), a Gaussian filter is applied in the horizontal direction. In the vertical direction, the use of finite differences is equivalent to a top-hat filtering, where the top-hat function would be $G \equiv 1/\Delta$ for points within a distance Δ and zero outside.

The size of the filter is $\Delta = 2\Delta x$, where Δx is the horizontal grid spacing (see Table 1). The field component u_i can be thus decomposed as

$$u_i = \overline{u}_i + u_i'', \tag{4}$$

similarly for the temperature field θ. After applying the filter operator both to the equations for the velocity and for the potential temperature, and exploiting a decomposition of the form (4) for the advection terms, we obtain the following filtered equations:

$$\frac{\partial \overline{u}_i}{\partial t} = -\frac{\partial \overline{\overline{u}_i \overline{u}_j}}{\partial x_j} - \frac{\partial \tau_{ij}^{(u)}}{\partial x_j} - \frac{1}{\rho}\frac{\partial \overline{p}}{\partial x_i} + g_i \frac{\overline{\theta}}{\theta_0}\delta_{i3} - f\epsilon_{ij3}\overline{u}_j + \nu\nabla^2\overline{u}_i, \tag{5}$$

$$\frac{\partial \overline{u}_i}{\partial x_i} = 0, \tag{6}$$

$$\frac{\partial \overline{\theta}}{\partial t} = -\frac{\partial \overline{\overline{u}_i \overline{\theta}}}{\partial x_i} - \frac{\partial \tau_i^{(\theta)}}{\partial x_i} + \kappa\nabla^2\overline{\theta}, \tag{7}$$

where ρ is the air density, p is the pressure, f is the Coriolis parameter, ν is the molecular viscosity, κ is the thermal molecular diffusivity, $g_i(\overline{\theta}/\theta_0)\delta_{i3}$ is the buoyancy term, and θ_0 is a reference temperature. The quantities to be modeled in terms of large-scale fields are

$$\tau_{ij}^{(u)} = R_{ij} - R_{kk}\delta_{ij}/3, \quad \tau_i^{(\theta)} = \overline{\overline{\theta}\overline{u_i''}} + \overline{\theta''\overline{u}_i} + \overline{\theta''u_i''}, \tag{8}$$

where

$$R_{ij} = \overline{\overline{u}_i\overline{u_j''}} + \overline{\overline{u_i''}\overline{u}_j} + \overline{u_i''u_j''}. \tag{9}$$

Expressions (8) represent the subgrid-scale fluxes of momentum and heat, respectively. The following small-scale closures are adopted

$$\tau_i^{(\theta)} = -K_H\partial_i\overline{\theta}, \tag{10}$$

$$\tau_{ij}^{(u)} = -2\gamma K_M S_{ij} - SK_M'\langle S_{ij}\rangle. \tag{11}$$

In the first equation, K_H is the eddy diffusivity for the scalar θ. In the second equation, $S_{ij} = 1/2(\partial_i\overline{u}_j + \partial_j\overline{u}_i)$ is the strain tensor of the resolved field; K_M and K_M' are respectively the fluctuating and the mean-field eddy viscosity, and γ is the so-called isotropy factor. In addition to the filtered equations for the temperature $\theta(\mathbf{x})$ and the velocity field $\mathbf{u}(\mathbf{x})$, the LES code also solves the evolution equation for the SGS turbulent kinetic energy (Moeng 1984; Sullivan et al. 1994). For details we refer to Sullivan et al. (1994), where the two-part eddy viscosity model (11), has been introduced. Such closure permits to reach a better agreement between the mean wind and temperature profiles obtained in a LES, and their forms derived from similarity theory in the convective boundary layer (CBL). Moreover, it has been widely tested and employed to investigate basic research problems in the framework of boundary layer flows (see Moeng and Sullivan 1994; Antonelli et al. 2003, among others). The LES numerical code used for this work is from the National Center for Atmospheric Research (NCAR), plus minor modifications to perform online and offline statistical analysis.

3. Numerical experiments

For the present study, we have performed two convective experiments characterized by different ratios between the buoyancy and the shear production terms. The physical parameters are listed in Table 1. As is well known, the stability parameter $\zeta = -z_i/L_{\mathrm{mo}}$, where z_i is the mixed layer height and L_{mo} is the Monin–Obukhov length, provides a measure of the atmospheric stability. According to Deardorff (1972), a convective regime settles in if $\zeta > 4.5$. From the values reported in Table 1, experiment 2 with $\zeta = 164$ corresponds to a pure buoyancy dominated regime; experiment 1, with $\zeta = 5.3$, while still being in a convective regime, is also affected by a relatively small shear.

We mention that our experiment 1 has a degree of convection in between experiment B and experiment SB1 described by Moeng and Sullivan (1994). Our experiment 2 is similar to experiment 1 by Nieuwstad and Brost (1986): but, differing from theirs, which is a decaying experiment, we maintain a constant heat flux from the bottom boundary for the entire duration of the simulation. A quasi steady state is thus reached in our experiments.

It is worth observing that the application of the LES strategy is very robust in convective situations, as the present cases. On the contrary, it may become questionable in stratified boundary layers where turbulence can attain scales small in comparison to the filter length-scale Δ (Mason 1994).

The numerical simulations have been performed on a homogeneously spaced $NX \times NY \times NZ = 256^3$ cubic lattice, biperiodic in the horizontal plane. The code is pseudospectral in the xy plane, and it is discretized with finite differences in the vertical direction (first-order discretization); time integration is performed using a third-order Runge–Kutta algorithm (Spalart et al. 1991). Runs have been performed on an IBM-SP4 parallel computer at the Italian interuniversity consortium CINECA, using 16 processors for a total duration of about 150 hours per process for each experiment.

After a time $t_0 \sim 8\tau*$, where $\tau*$ is the large-scale eddy turnover time since the beginning of the simulation, the systems reached a well-defined quasi steady state. In Fig. 1, we can see the evolution of the mixed layer for $t > t_0$. The quasi steady state is defined from the linear rate of growth of the temperature field inside the mixed layer, shown in Fig. 2. Another proof of quasi stationarity is given by the behavior of the temperature flux $\langle w'\theta'\rangle$, averaged in the horizontal plane and for a duration time of $\sim\tau*$, which shows the expected profile with the height (plotted in Fig. 3). Vertical profiles of the wind speed are also given in Fig. 4.

All the forthcoming analysis has been carried out within the mixed layer, collecting data for $t > t_0$. The total time of the simulation T, which does not include the transient, and the sampling time t_{samp} are also listed in Table 1. In both experiments, the inertial range extension is about $0.015 \leq r/L \leq 0.12$, L being the side of the numerical domain, that is, twice the integral scale of the system (see sections 4a and 4b). It corresponds to a range of about 5–6 to 30 mesh spacings for both the velocity and temperature fields.

Different from what happens in the horizontal plane, statistics in the vertical plane are not everywhere ho-

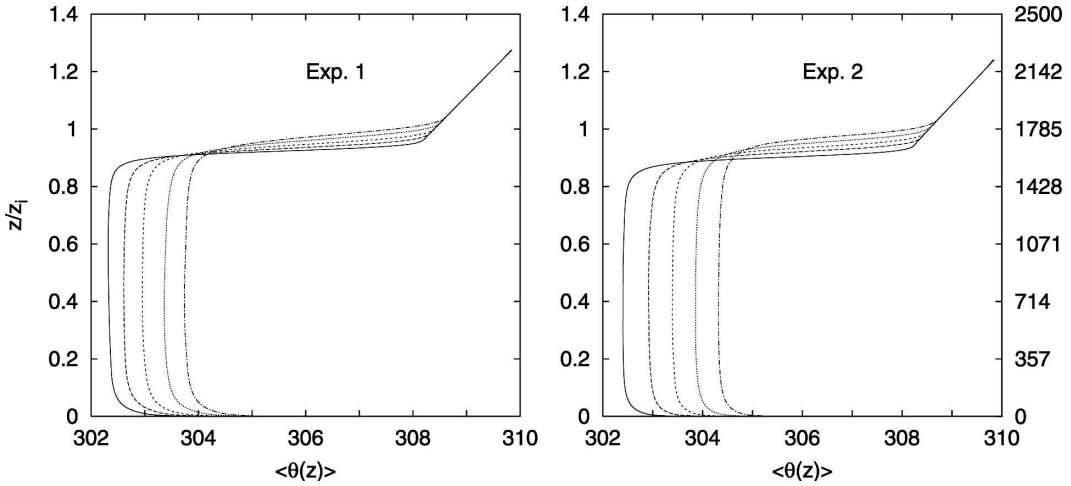

FIG. 1. Vertical profiles of the mean potential temperature for both experiments. Temperature is expressed in K. The curves, equispaced in time of about $4\tau*$, give the evolution of the potential temperature during the numerical simulation, after the quasi steady state was reached. The left y axis of each plot is expressed in dimensionless units z/z_i; the rightmost y axis gives the vertical extension of the physical domain, expressed in m.

mogeneous because of the boundaries. It is thus necessary to restrict our attention to the region where the mixing is such that the turbulent fields can be considered almost homogeneous. From the mean temperature profile, such sublayer approximately extends from $h = 390$ m to $h = 1270$ m: here deviations from the mean temperature, measured at the center of the mixed layer, were smaller than 0.1%.

4. Anisotropic behavior of small-scale fluctuations: Standard analysis

The atmospheric boundary layer is affected by strong inhomogeneities coupled with strong anisotropies, due to the external mechanisms driving the turbulence and to the presence of the boundaries. Concerning the issue of isotropy restoration in the inertial range, the situation is the following: a large number of experimental and numerical studies, performed in the last fifteen years, indicated that anisotropy might persist, in contrast with the classical picture of local statistical isotropy and universality of inertial range turbulence (Pumir and Shraiman 1995; Warhaft 2000). For example, it has been commonly observed that increment skewness factors [defined in (12)] do not really decrease and eventually increase with the scale $|\mathbf{r}|$, as this becomes smaller and smaller compared to the large scale of the system L (see Sreenivasan and Antonia

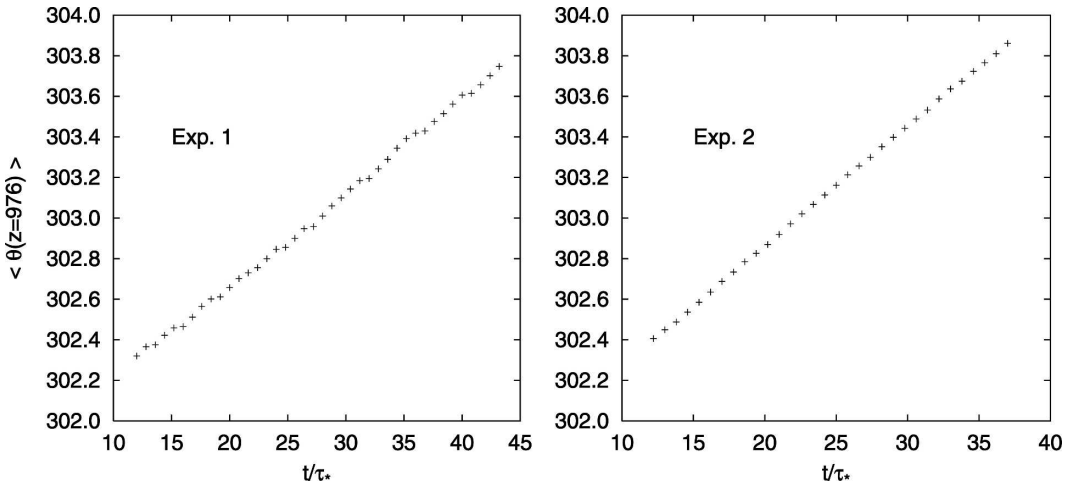

FIG. 2. Time evolution of the mean potential temperature at a specific height $h_0 \sim 976$ m, well inside the mixed layer, after the quasi steady state has been reached. Time is expressed in large-eddy turnover time $\tau*$ units. Temperature is expressed in K.

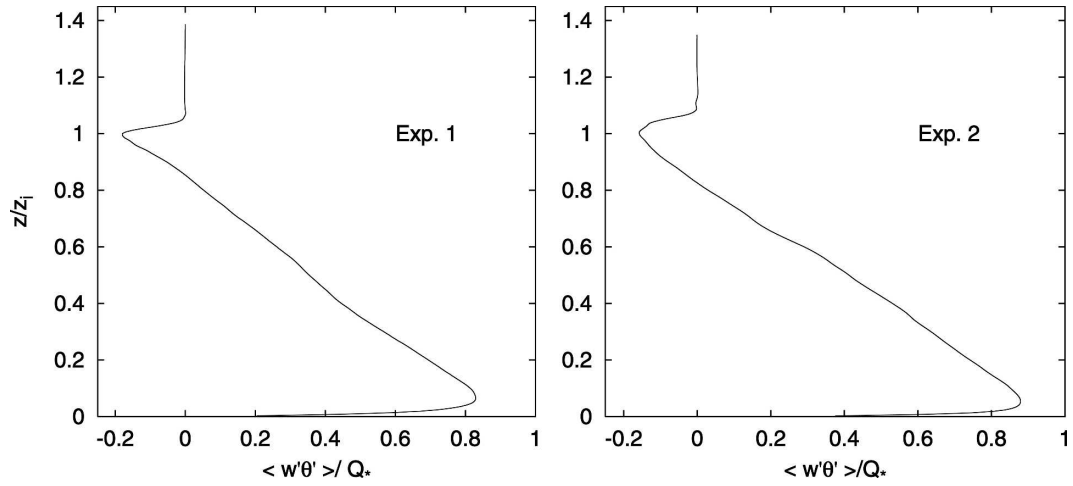

FIG. 3. Vertical profile of the heat flux for both experiments.

1997; Shen and Warhaft 2000). A deeper comprehension of these puzzling results has been recently achieved, when it has been recognized that the persistence of anisotropies is due to the simultaneous presence of intermittency and anisotropic effects (see, e.g., Biferale and Vergassola 2001). Since intermittency makes anisotropic fluctuations decay slower than what predicted by dimensional analysis, we can measure some anisotropic observables which do not vanish going at smaller scales, or at increasing Reynolds number. However, if the two effects are properly disentangled, it becomes clear that anisotropic fluctuations are subleading, or subdominant, with respect to isotropic ones. The common understanding is thus that isotropy is statistically recovered, at scales well separated from the large ones and the boundaries.

This is confirmed by in situ experiments also. Experimental PBL measurements performed in nearly neutral conditions and at a microscale Reynolds number $\mathrm{Re}_\lambda \sim 10\,000$, have shown that the velocity field (Kurien et al. 2000), and the temperature field (Kurien et al. 2001), while affected by strong anisotropies on the outer scales of turbulence, possess a trend toward isotropy with decreasing scales. Such trend differs from that expected by classical (Kolmogorov theory) dimensional arguments, and the reported persistence of anisotropies is due to the presence of intermittency. Kolmogorov isotropy restoration hypothesis—slightly modified because of intermittency—finds an experimental confirmation.

Similar questions can be asked in the LES framework. In section 5, the notion of isotropy restoration will be clearly stated. Here, we start by a general description of temperature and velocity field statistics, trying to identify the anisotropic and intermittency properties of turbulent fluctuations.

a. Temperature statistics

For both experiments, we look at the probability density functions $P[\delta_r\,\theta(\mathbf{x})]$ of scalar differences,

$$\delta_r\theta(\mathbf{x}) \equiv \theta(\mathbf{x}+\mathbf{r}) - \theta(\mathbf{x}),$$

at scale r. Temperature fluctuations depend on the kind and on the intensity of the external forcing mechanisms. For linear systems (Shraiman and Siggia 2000; Falkovich et al. 2001), the existence of universal scaling exponents, together with PDFs with nonuniversal shapes, have been shown. Whether such findings are valid also in nonlinear systems, such as for example the CBL, is still an open problem.

In Fig. 5, we consider the PDFs $P(\delta_r\theta)$, normalized with their variance, at four different scales r/L spanning the inertial subrange. The vector $\mathbf{r}$ is chosen in the horizontal plane, where the field is homogeneous, and we

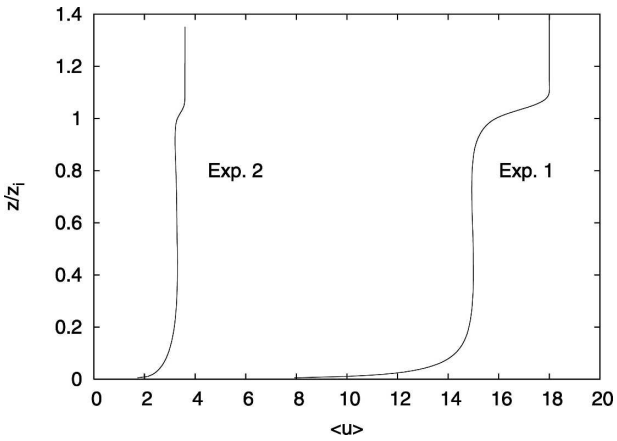

FIG. 4. Comparison of the vertical profile of the wind speed for both experiments. The wind speed is expressed in m s^{-1}.

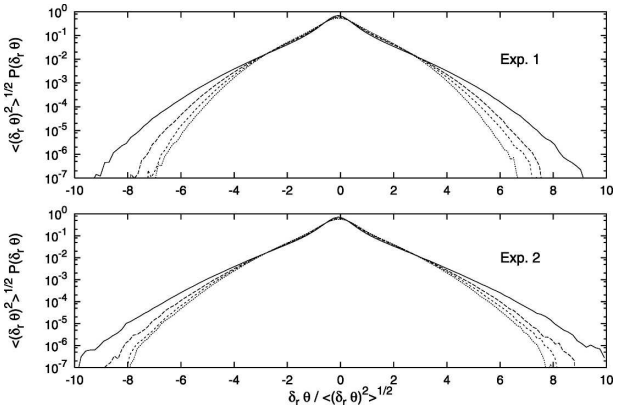

FIG. 5. PDFs of the potential temperature field increment $P(\delta_r\theta)$, normalized with their standard deviations, for both experiments. Temperature increments are measured in the horizontal plane *xy,* at four different scales: $r/L = 0.02$, $r/L = 0.04$, $r/L = 0.06$, and $r/L = 0.1$. Inner curves refer to larger scale r/L ratios. At the largest scales (not shown), the PDF has super-Gaussian tails.

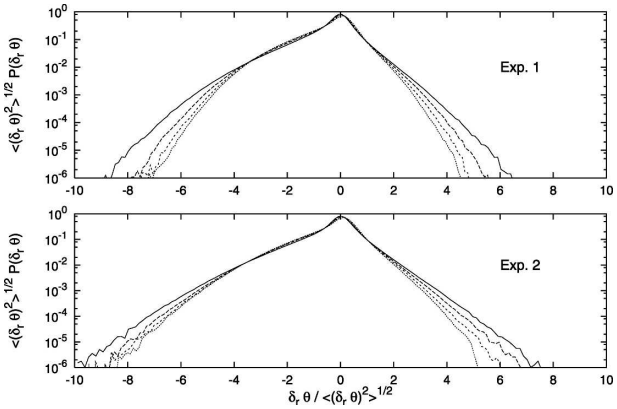

FIG. 6. PDFs of potential temperature increment $P(\delta_r\theta)$ measured in the vertical plane *yz,* normalized with their standard deviations. The curves (from outer to inner) refer to increments measured at four different scales: $r/L = 0.06$, $r/L = 0.1$, $r/L = 0.14$ and $r/L = 0.18$.

can thus disregard the **x** dependence. As expected, the PDFs of the two experiments have different shapes, since they have to match different large-scale conditions. Within each experiment, we notice that as the scale r/L decreases, the curves possess broader and broader tails, but they seem only slightly asymmetric. The curves are significantly super Gaussian, exhibiting nonnegligible fluctuations as large as ~8−10 root-mean-square (rms) values. In addition, the curves even if rescaled with their variance do not collapse, which is evidence that the two experiments are both strongly intermittent (Frisch 1995). The same analysis can be repeated considering temperature increments measured in the vertical plane *yz*, normal to the mean flow, in the subregion where the influence of the inhomogeneity is not too strong (as discussed in the previous section). As it is evident from Fig. 6, the PDFs now exhibit a much higher degree of asymmetry for both experiments. In Fig. 7, we plot the behavior of the increment kurtosis $K^\theta(\mathbf{x}, \mathbf{r}) \equiv \langle[\delta_r\theta(\mathbf{x})]^4\rangle/\langle[\delta_r\theta(\mathbf{x})]^2\rangle^2$, defined in terms of the structure functions $S^{(p,\theta)}(\mathbf{x}, \mathbf{r}) \equiv \langle[\delta_r\theta(\mathbf{x})]^p\rangle$. Here we consider only the structure functions measured in the horizontal plane, along the direction at 45°.[1] The inertial range, delimited by the vertical lines in the figure, extends from r/L ~0.015 to r/L ~0.12. The kurtosis, even at large scales where it saturates to a constant, is very far from the Gaussian value ~3. The scale dependence of $K^\theta(r)$, together with its deviation from the Gaussian value even at large scales, is another indication that the temperature field is intermittent, but we see no big differences from one experiment to the other.

The anisotropic properties of the temperature field can be conveniently quantified in terms of the behavior of the odd-order structure functions $S^{(2p+1,\theta)}(\mathbf{x}, \mathbf{r})$. Indeed, for an isotropic scalar field, the PDF should be symmetric; equivalently, odd order moments should be identically zero. We consider the quantities defined as

$$\sum\nolimits^{\theta}_{(2p+1)}(\mathbf{x}, \mathbf{r}) \equiv \frac{S^{(2p+1,\theta)}(\mathbf{x}, \mathbf{r})}{[S^{(2,\theta)}(\mathbf{x}, \mathbf{r})]^{(2p+1)/2}}. \qquad (12)$$

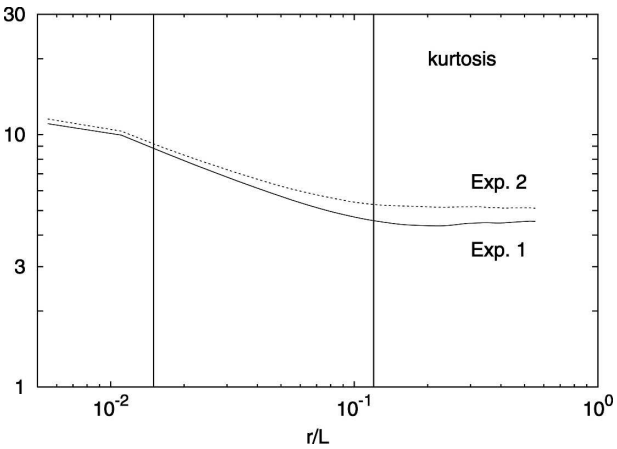

FIG. 7. Log–log plot of the potential temperature field increment kurtosis $K^\theta(r) = \langle(\delta_r\theta)^4\rangle/\langle(\delta_r\theta)^2\rangle^2$, calculated in the horizontal plane *xy*. The vertical lines delimit the inertial range extension, defined in section 3.

[1] Following Celani et al. (2001), this choice is done to reduce the anisotropic effects in the horizontal plane. In particular structure functions $S^{(p)}(\mathbf{r}) \equiv \langle[\theta(\mathbf{x} + \mathbf{r}) - \theta(\mathbf{x})]^p\rangle$ are measured by choosing the increment vector **r** in the horizontal plane and oriented along the diagonal such that $\hat{\mathbf{r}} = (\pm 1, \pm 1, 0)$.

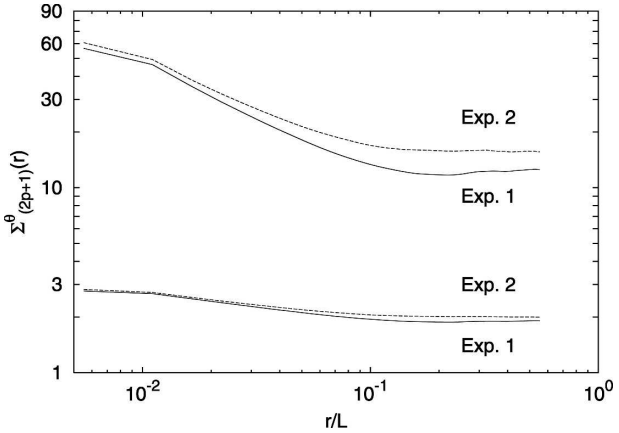

FIG. 8. Log–log plot of the potential temperature field increment skewness $\Sigma^{\theta}_3(r) = \langle(\delta_r\theta)^3\rangle/\langle(\delta_r\theta)^2\rangle^{3/2}$ (lower curves) and hyperskewness $\Sigma^{\theta}_5(r) = \langle(\delta_r\theta)^5\rangle/\langle(\delta_r\theta)^2\rangle^{5/2}$ (upper curves). Both indicators are calculated in the horizontal plane *xy*.

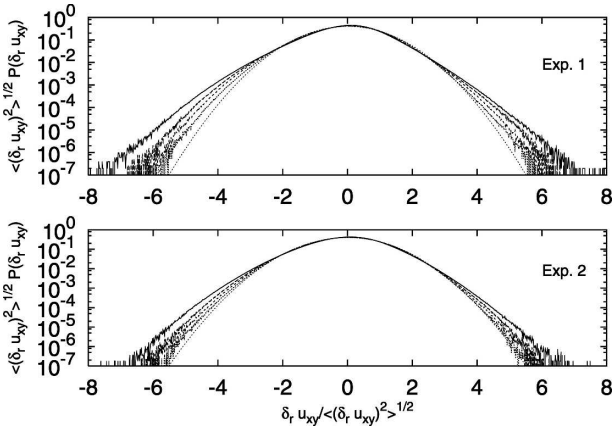

FIG. 9. PDFs of velocity increments $P(\delta_r u_{xy})$ measured in the horizontal plane, at four different scales: $r/L = 0.02$, $r/L = 0.04$, $r/L = 0.06$, and $r/L = 0.1$. A normal distribution is also plotted for comparison (internal dotted curve). At the largest scales, the PDF approaches a Gaussian distribution.

For $p = 1$ and $p = 2$, they are the increment skewness and hyperskewness coefficients, respectively. By local isotropy hypothesis, these are expected to be zero for small $|\mathbf{r}|/L$ or to decrease rapidly with diminishing scale in the inertial subrange. Our measurements, in agreement with numerical (Pumir and Shraiman 1995) and experimental results (see Kurien et al. 2001; Warhaft 2000, for a recent review), show that the skewness coefficients essentially remain $O(1)$, almost independent of the scale separation (see Fig. 8).

As long as we consider low-order moments, as for the kurtosis before, there are no evident differences between experiment 1 and 2. Differences appear when we measure large fluctuations, like those associated with the hyperskewness $S^{(5,\theta)}/(S^{(2,\theta)})^{5/2}$. Also we notice that the hyperskewness coefficients tend to increase for small r/L, another effect due to intermittency. How to disentangle anisotropy and intermittency, by means of the SO(3) decomposition, will be the subject of section 5.

b. Velocity statistics

We apply the previous analysis to the velocity field, also. As before, we separate the measurements in longitudinal horizontal increments $\delta_r u_{xy} \equiv [\mathbf{u}(\mathbf{x} + \mathbf{r}) - \mathbf{u}(\mathbf{x})] \cdot \hat{\mathbf{r}}$, with $\hat{\mathbf{r}}$ belonging to the *xy* plane, and in longitudinal vertical increments $\delta_r u_{yz}$ where $\hat{\mathbf{r}}$ is taken in the vertical *yz* plane. In Figs. 9 and 10, the PDFs of horizontal and vertical velocity increments are shown: these change shapes when changing the large-scale conditions (experiment 1 or experiment 2). But, unlike the temperature case, there are no big differences between the horizontal and vertical plane statistics. As it is known from many experimental and numerical results (see Sreenivasan and Antonia 1997), the velocity field is less intermittent than the temperature field. This observation is valid in our case also, since we have that for both experiments the velocity increment PDFs become almost Gaussian at large separations. In addition, they appear more symmetric than those of the temperature field. The lower intermittency and the tendency toward a Gaussian distribution at large scale is confirmed by the behavior of the increment kurtosis measured in the horizontal plane, plotted in Fig. 11, which clearly saturates to the value 3 for large scales. As in Fig. 7, the inertial range is delimited by the vertical lines and extends from $r/L \sim 0.015$ to $r/L \sim 0.12$.

Odd order moments, measured in the horizontal plane, are plotted in Fig. 12. Two observations are in order. The first is that also for the velocity field the increment skewnesses $\Sigma^u_3(r)$ essentially remain $O(1)$, almost independent of the scale separation. The second is that, as quantified by the value of the $\Sigma^u_3(r)$ and $\Sigma^u_5(r)$ coefficients, the velocity field appear to be less anisotropic than the potential temperature field.

From a qualitative point of view, the two experiments characterized by a different degree of convection exhibit similar scaling properties for the kurtosis or the skewness factors, either for the velocity and the temperature fields. Still, it is difficult to comment on the universality and the isotropy issues, mainly because in the previous analysis intermittency and anisotropic effects are mixed together.

5. How to disentangle anisotropic contributions: The SO(3) decomposition

The importance of properly disentangling isotropic and anisotropic fluctuations has been demonstrated in

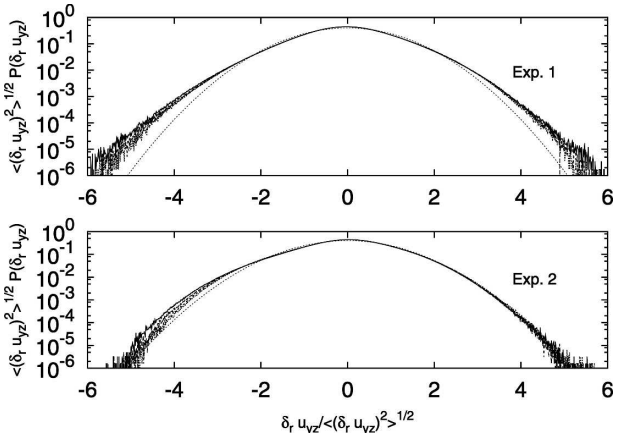

FIG. 10. PDFs of velocity increments $P(\delta_r u_{yz})$ measured in the vertical plane *yz,* at four different scales: $r/L = 0.15$, $r/L = 0.18$, $r/L = 0.23$, and $r/L = 0.27$. Inner curves refer to larger r/L ratios. A normal distribution is also plotted for comparison (internal dotted curve).

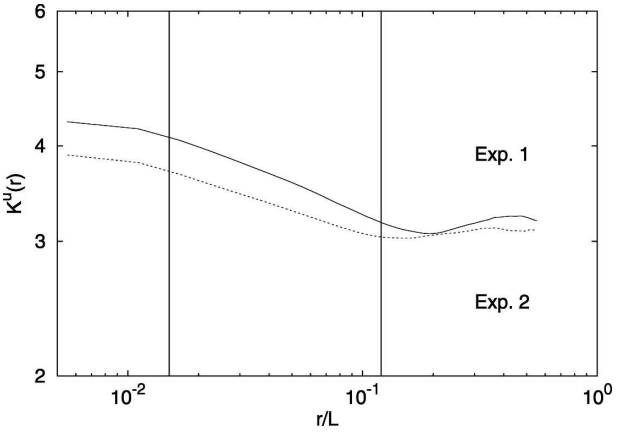

FIG. 11. Log–log plot of the velocity field increment kurtosis $K^u(r) = \langle(\delta_r u_{xy})^4\rangle/\langle(\delta_r u_{xy})^2\rangle^2$, calculated in the horizontal plane *xy,* from $r \ll L$ to larger scales. The vertical lines delimit the inertial range extension.

the analysis of the statistical properties of inertial range turbulence in many different contexts (Biferale and Procaccia 2005). Investigating and developing proper small scale models for anisotropic turbulence is also a first-order question appearing in large-eddy simulations of turbulent flows affected by anisotropic body forces (see Meneveau and Katz 2000). As firstly highlighted by Arad et al. (1999a), anisotropy can be studied by means of a decomposition of the physical observables onto the irreducible representations of the rotational symmetry group SO(3). The physical basis of this approach relies on the observation that anisotropic external forcings driving the turbulence should have their dominant contribution at large scales: inertial range quantities should then be statistically independent of them and thus rotationally invariant. In linear systems of passive transport and in the pure Navier–Stokes problem, in the presence of large-scale forcing, experimental and numerical results support the validity of this approach (Biferale and Procaccia 2005). Also, applications of the SO(3) decomposition reveal that separating the isotropic behavior from the anisotropic ones clearly improves the understanding of the inertial range statistical properties and their comparison with classical dimensional expectations (see Biferale et al. 2002). Concerning convection problems, the SO(3) decomposition has been fruitfully applied by Biferale et al. (2003), in a direct numerical simulation of a homogeneous Rayleigh–Bénard cell, and in PBL field experiments on the available anisotropic fluctuations measured by two anemometers (Kurien et al. 2000, 2001).

Here we will not review the theoretical basis and the technical details of the SO(3) approach. What is of interest for us is to say that we can apply it either to correlation or structure functions; that is, scale-dependent averaged quantities, to separate the statistical behavior of the isotropic fluctuations from the anisotropic ones. From a practical point of view, we can look at it as to the most appropriate projection basis for anisotropic observables, making the decomposition sketched in (2) systematic.

We focus on scalar quantities, such as the temperature structure functions $S^{(p,\theta)}(\mathbf{r})$ and the velocity longitudinal structure functions, $S^{(p,u)}(\mathbf{r})$, which have a simple representation [the interested reader can refer to Arad et al. (1999a) for a thorough description]. Their decomposition is just

$$S^{(p)}(\mathbf{r}) = \sum_{j=0}^{\infty} \sum_{m=-j}^{j} S_{jm}^{(p)}(r) Y_{jm}(\hat{\mathbf{r}}), \tag{13}$$

where the indices (j, m) of the spherical harmonics $Y_{jm}(\hat{\mathbf{r}})$ label the total angular momentum and its projection on a reference axis, respectively. The isotropic sector, labeled $(j, m) = (0, 0)$, is associated with the fundamental harmonic $Y_{00}(\hat{\mathbf{r}}) = 1/(4\pi)$; the degree of anisotropy increases with $j > 0$. The spherical harmonics form a complete basis to project three-dimensional objects. It is worth saying that for the SO(2) rotational group, that is the decomposition in a $d = 2$ space, the most natural basis would be the set of functions $\cos(j\phi)$, $\sin(j\phi)$.

The role of the decomposition is, by means of the appropriate complete basis functions, to disentangle vector dependent quantities such as $S^{(p)}(\mathbf{r})$, separating the angular from the pure scaling information, contained in $S_{jm}^{(p)}(r)$. Focusing on the statistical properties in

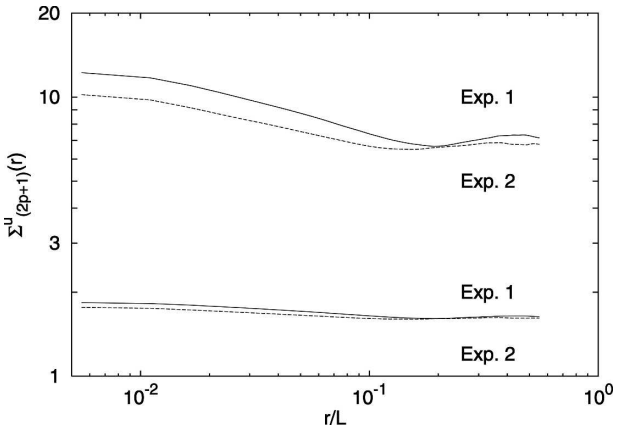

FIG. 12. Log–log plot of the velocity field increment skewness $\Sigma^u_3(r) = \langle(\delta_r u_{xy})^3\rangle/\langle(\delta_r u_{xy})^2\rangle^{3/2}$ (lower curves) and hyperskewness $\Sigma^u_5(r) = \langle(\delta_r u_{xy})^5\rangle/\langle(\delta_r u_{xy})^2\rangle^{5/2}$ (upper curves) calculated in the horizontal plane xy.

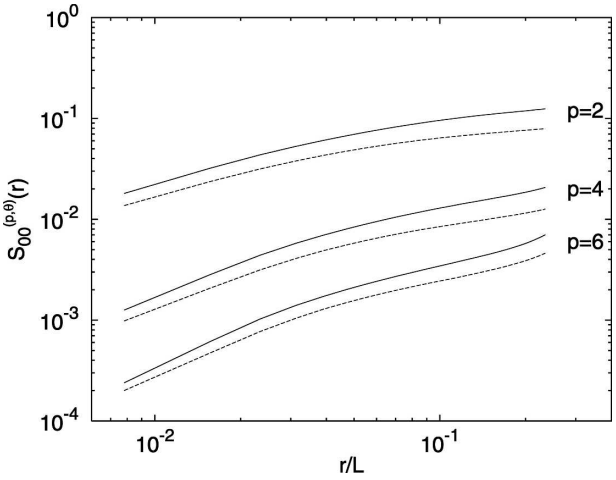

FIG. 13. Potential temperature field. Log–log plot of the isotropic projections $S_{00}^{(p,\theta)}(r)$ for the structure functions of order $p = 2$, 4, 6, for both experiments. At any order, the curves above (continuous lines) refer to experiment 1; the curves below (dashed lines) refer to experiment 2.

the inertial range of scales, we look for a scaling behavior of the form $S_{jm}^{(p)}(r) \sim c_{jm} r^{\xi^j(p)}$, with a different $\xi^j(p)$ exponent characterizing each anisotropic sector. The general expectation is that the coefficients c_{jm} should be strongly dependent on the anisotropic properties of the large-scale physics, while the values of the scaling exponents, $\xi^j(p)$, should be independent of the large-scale forcing and/or boundary conditions, thus enjoying a much higher degree of universality. Such a picture can be proved on a rigorous basis for the so-called Kraichnan models (Kraichnan 1994), that is, linear problems of passive advection by Gaussian, synthetic velocity fields [see Falkovich et al. (2001) for a recent review], but its validity is thought to go beyond this class of stochastic models and beyond linear problems (Biferale and Procaccia 2005).

We come to the issue of isotropy restoration. Expressed in terms of the behavior of the anisotropic projections, it corresponds to the existence of a hierarchical organization of the different scaling exponents for the structure functions $S^{(p)}(\boldsymbol{r})$ of any order p:

$$\xi^{j=0}(p) \le \xi^{j=1}(p) \le \xi^{j=2}(p) \le \ldots \le \xi^j(p). \quad (14)$$

Indeed, this means that going to scales r much smaller than the integral scale L, the pth order structure function will be dominated by the fluctuation having the smallest scaling exponent; that is, the isotropic one of exponent $\xi^{j=0}(p)$. Compared to the isotropic fluctuations, the anisotropic ones give subleading (i.e., negligible) contributions for decreasing $|\mathbf{r}|$: the higher is the order j of the projection, the more subleading is the correspondent anisotropic fluctuation.

In the case of Kraichnan models, it has been rigorously proved that, in the presence of large-scale anisotropic forcings, a hierarchy like (14) exists and isotropy is statistically restored in the inertial range (Lanotte and Mazzino 1999; Arad et al. 2000). Beyond Kraichnan models and analytic proofs, similar evidences have been found experimentally and numerically in realistic turbulent systems, both for the temperature field (Biferale et al. 2003), and the velocity field (Biferale et al. 2002; Kurien et al. 2000). Clearly more results are needed, but isotropy restoration seems a common feature of turbulent inertial range statistics.

Below, we will compare the isotropic and the anisotropic projections of the two experiments, and possibly give an answer to the problems of the universality and the statistical restoration of isotropy for turbulent fields.

It is worth recalling that, while we have a systematic procedure to disentangle anisotropic statistical fluctuations [i.e., the SO(d) decomposition], we do not have a similar tool for inhomogeneous systems. In the latter case, no systematic approach is available to identify the different contributions to the statistics due to inhomogeneity. Moreover, close to the boundaries, LES fields are very sensitive to the SGS modeling. In view of these considerations, we applied the SO(3) decomposition to the part of the mixed layer where the z dependency of statistical observables turns out to be negligible, as discussed before.

a. Temperature statistics

In Fig. 13, we show the isotropic projections $S_{00}^{(p,\theta)}(r)$ for the even structure functions of order $p = 2$, 4, 6 for

experiments 1 and 2. We did not consider odd order moments, since these are very noisy due to cancellations.

At large scales, the temperature statistics have to match with different conditions in the two experiments, but for smaller scales, we observe that the two curves have compatible power-law behaviors at each order p. Identical scaling exponents for the isotropic projections would mean that the temperature statistics are universal with respect of the forcing mechanisms. In our case, we measure differences of the order of the error bars between the scaling exponents of the experiment 1 and experiment 2 (in the scaling region, error bars are estimated by extracting the maximal and minimal slope fitting the expected power-law behavior and are of the order of 25% of the value of the estimated exponent). Experiments with a larger inertial range of scales should be performed to have a precise measure of these possible small differences. However, within the present finite-size limits and error bars, these results are consistent with a weak or no dependence, of the isotropic projections, on the degree of convection.

Concerning anisotropic contributions, we apply the decomposition (13) to measure the anisotropic projections of moments of order $p = 2$. Those of order $p > 2$ soon become noisy and thus poorly informative. It is worth saying that the observed noise is not due to limited statistics, since the isotropic projections of moments up to order $p = 6$ show a very clean behavior, but rather to the limitation of the interpolation scheme of the spherical harmonics (see below) and to finite size effects.

Figures 14 show the behavior of the ratio $A^{\theta}(r) \equiv S_{jm}^{(2,\theta)}(r)/S_{00}^{(2,\theta)}(r)$, of the most energetic anisotropic projection, in our case $(jm) = (22)$, to the isotropic one, for the second-order structure function.

The first point of each curve is not to be considered: it clearly suffers from the interpolation scheme.[2] The ratio $A^{\theta}(r)$ is a quantitative indicator of the anisotropy degree, and accordingly we refer to it as anisotropy index.

First, we notice that, at any scale, $A^{\theta}(r) < 1$: this implies that even the most energetic anisotropic fluctuation gives a contribution much smaller than the isotropic one. Second, we notice that, for both experiments, $A^{\theta}(r)$ is an increasing function of r (except at large scale, due to the shape of the spherical harmonic and the large-scale constraint). This means that the considered anisotropic projection has a higher exponent than the isotropic one, or equivalently that the anisotropic exponent $\xi^{22}(2,\theta)$ is subleading with respect to the isotropic one $\xi^{00}(2,\theta)$, for any of the two experiments. This property is actually observed for all the measured sectors, precisely those labeled by $j = 2$ and $j = 4$, with $m \in [-j; j]$. In the same figure, we plot as an example also the behavior of the ratio $S_{42}^{(2,\theta)}(r)/S_{00}^{(2,\theta)}(r)$. In the light of the comments made in section 5, the above results mean that isotropy is recovered in the inertial range, in agreement with general observations in PBL field experiments.

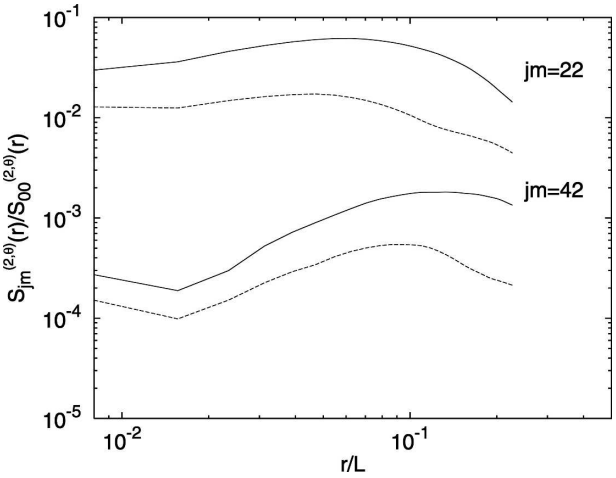

FIG. 14. Potential temperature field. Log–log plot of the ratio between an anisotropic projection to the isotropic one $S_{22}^{(2,\theta)}(r)/S_{00}^{(2,\theta)}(r)$, for both experiments. The same for the ratio $S_{42}^{(2,\theta)}(r)/S_{00}^{(2,\theta)}(r)$ is also plotted; these curves have been slightly shifted below for plotting reasons. For each choice of the jm sector, the curves above (continuous lines) refer to experiment 1; the curves below (dashed lines) refer to experiment 2.

b. Velocity statistics

The same analysis can be repeated for the velocity field. We start by looking at the isotropic components $S_{00}^{(p,u)}(r)$ of the structure functions of order $p = 2, 4, 6$, plotted in Fig. 15. As already mentioned, the velocity field is known to be much less intermittent than the temperature field. This amounts to saying that, for any fixed order p, the statistical convergence of the structure function is reached sooner for the velocity than for temperature field. Even if the scaling region is narrow, the curves for the two experiments show similar scaling behavior, with no detectable difference at any order $p \in [2, 6]$. This is the fingerprint of universality with respect to the degree of convection.

Concerning the anisotropic sectors, in Fig. 16, we

[2] The extraction of the projections onto the spherical harmonics, $S_{jm}^{(p)}(r)$, implies the calculus of an integral over a sphere of radius r. Working on a cubic grid, we have to approximate the sphere with the nearest cube. Clearly, for smaller radius, we have fewer grid points to interpolate with.

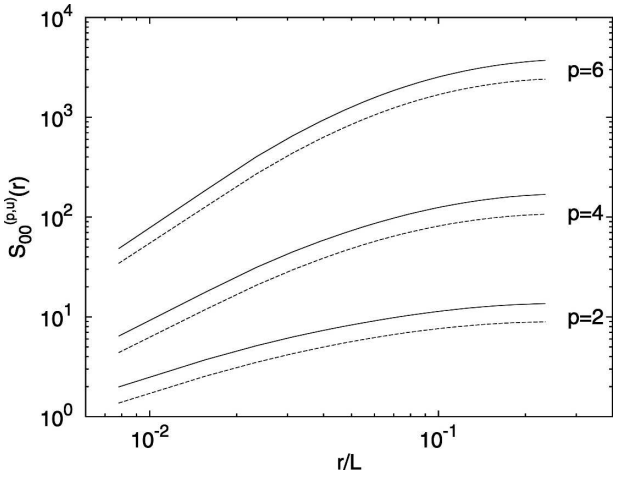

FIG. 15. Velocity field. Log–log plot of the isotropic projections $S_{00}^{(p,u)}(r)$ for the structure functions of order $p = 2, 4, 6$. At any order, the curves above (continuous lines) refer to experiment 1; the curves below (dashed lines) refer to experiment 2.

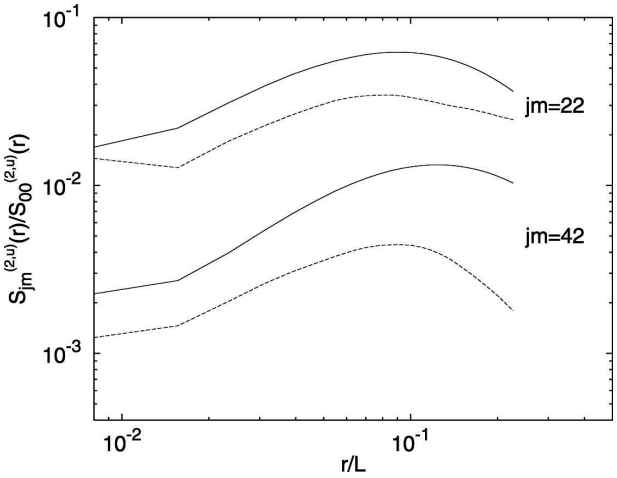

FIG. 16. Velocity field. Log–log plot of the ratio between an anisotropic projection to the isotropic one $S_{22}^{(2,u)}(r)/S_{00}^{(2,u)}(r)$, for both experiments. The same for the ratio $S_{42}^{(2,u)}(r)/S_{00}^{(2,u)}(r)$, is also plotted. As in Fig. 14, the curves above (continuous lines) refer to experiment 1; the curves below (dashed lines) refer to experiment 2.

plot the anisotropy index $A^u(r) \equiv S_{jm}^{(2,u)}(r)/S_{00}^{(2,u)}(r)$ versus r/L, for the most energetic fluctuation $(jm) = (22)$, and for the sector $(jm) = (42)$. Conclusions similar to those of the temperature field can be drawn for the velocity field, pointing to the statistical isotropy restoration.

6. Sensitivity test at higher resolution

In this section we address the issue of the possible influence of SGS terms on the obtained results. Two different tests might be performed for such purpose. The first consists in performing simulations with different closure schemes; the second is to increase the resolution and thus to push at smaller and smaller scales the effect of SGS modeling. Since we are interested in assessing inertial range properties rather than contrasting different SGS model, we choose the latter. Furthermore, with an increased resolution we can control other spurious effects as, for example, finite size effects, to which we referred previously.

We studied another classical experiment, namely the well-known experiment B by Moeng and Sullivan (1994), at two different resolutions: $N^3 = 256^3$ (we refer to it as experiment B_{256}), and $N^3 = 512^3$ (experiment B_{512}). For a detailed description of this case study, the reader is referred to the above mentioned paper. Here we only give some of the relevant physical parameters characterizing the experiment. The domain extension is $L_x = L_y = 5000$ m and $L_z = 2000$ m; the heat flux from the bottom boundary is $Q_* = 0.24$ km s^{-1}; the geostrophic wind is $U_g = 10$ m s^{-1}; the roughness length is $z_0 = 0.16$; the mixed layer depth are $z_i = 1030$ m and $z_i = 1500$ m, for experiment B_{256} and experiment B_{512}, respectively; the stability parameter is about $-zi/L_{\mathrm{mo}} = 18$; the convective velocity scale is $w_* = 2.0$ m s^{-1}; the friction velocity is $u_* = 0.56$ m s^{-1}; the large-scale eddy turnover time, estimated as $\tau_* \equiv z_i/w_*$, is about 510 s for the experiment B_{256} and 750 s for the experiment B_{512}, respectively.

After a well-defined quasi steady state was reached, we collected statistics for several large-scale eddy turnover times at resolution $N = 256^3$, and for one large-scale eddy turnover time for $N = 512^3$. On the SP4-IBM SP Power4 platform, it took 1 h to advance 1 h of simulation for the experiment B_{256}. At the higher resolution, such time became around an order of magnitude larger.

Coming to the results, skewness and hyperskewness coefficients, $\Sigma_{(2p+1)}(\mathbf{x}, \mathbf{r})$ with $p = [1, 2]$, are compared at the two resolutions in Figs. 17. For either the potential temperature field or the velocity field, we do not observe any significant difference in their inertial range statistical behavior when changing the resolution. Again we can improve our understanding by looking at the turbulent fluctuations with the SO(3) decomposition. In Fig. 18, we plot the isotropic sector curves for the second-order structure function. The power-law behavior of $S_{00}^{(2)}(r)$ does not change when increasing the resolution, for both the potential temperature and the velocity fields. In Fig. 19 we also show, for both fields and at the two resolutions, the anisotropy index $A(r) = S_{jm}^{(2)}(r)/S_{00}^{(2)}(r)$, in terms of the most energetic

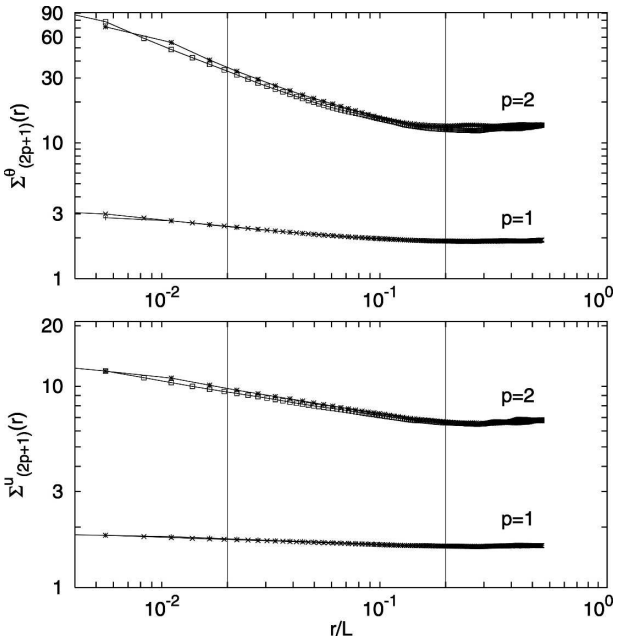

FIG. 17. (top) The top curves are the log–log plot of the hyperskewness coefficient $\Sigma^{\theta}_{5}(r) = \langle(\delta_r\theta)^5\rangle/\langle(\delta_r\theta)^2\rangle^{5/2}$ measured in experiment B_{256} (*) and experiment B_{512} (□). The bottom curves are the log–log plot of the potential temperature increment skewness coefficient $\Sigma^{\theta}_{3}(r) = \langle(\delta_r\theta)^3\rangle/\langle(\delta_r\theta)^2\rangle^{3/2}$ measured in experiment B_{256} (+) and experiment B_{512} (×). (bottom) The same but for the velocity field *u,* with the identical choice of symbols. Both indicators are calculated in the horizontal plane *xy*. The vertical lines define the inertial range extension common to both experiments.

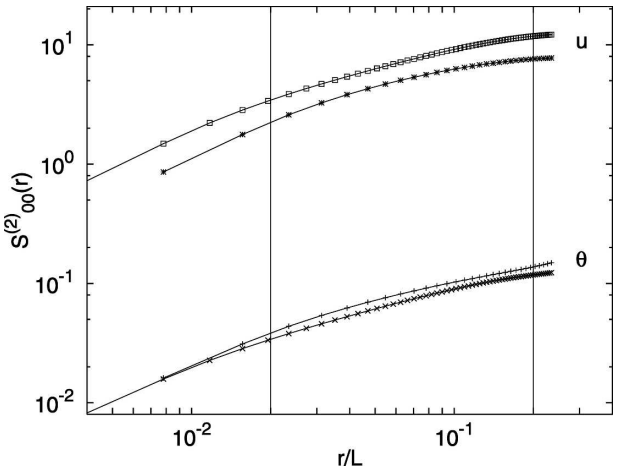

FIG. 18. Log–log plot of the isotropic projections of the structure functions of order $p = 2$ $S^{(p)}_{00}(r)$ for the potential temperature and the velocity fields, measured in the experiments experiment B_{256} and experiment B_{512}. For both the temperature and the velocity fields, the curves above refer to the experiment at moderate resolution 256^3; the curves below refer to the experiment at very high resolution 512^3. The vertical lines define the inertial range.

projection ($jm = 22$): similar qualitative behaviors are observed in experiment B_{256} and experiment B_{512}.

It is evident that increasing numerical resolution does not change the inertial range behavior of the considered structure functions, in particular those of the isotropic projections that by far exhibit the cleanest scaling. These findings corroborate the conclusions drawn from experiments experiment 1 and experiment 2 in the previous sections.

The robustness of the results can be actually understood by means of the following simple considerations. First of all, the uncertainties produced in a large-eddy simulation model by the SGS terms contaminate the turbulent fields in regions where small eddies dominate. This happens, for example, near a wall boundary and in the entrainment zone of the planetary boundary layer. On the contrary, in regions where energy-containing eddies are well resolved, as within the mixed layer where the present analysis has been focused, LES fields are known to be weakly dependent on the particular SGS scheme. Such dependence becomes even weaker in the case of convective boundary layers, as those here investigated, where the subgrid-scale motion acts as a net energy sink draining energy from the resolved motion. In other words, when the energy transfer is dominated by a direct cascade from large toward the small scales of motion, the cumulative (statistical) effect of the latter scales can be successfully captured by means of simple eddy-diffusivity/viscosity SGS models.

Moreover, we focused on scales of motion always larger than six or eight grid points; that is, sufficiently far from the lowest still resolved scales, that (a priori) might be dependent on parameterization schemes.

7. Conclusions

We have performed two high-resolution (256^3) numerical experiments of the CBL dynamics, using the large-eddy simulation technique. From our observations, we have clear evidences that isotropy is restored at inertial range scales for both the temperature and the velocity fields. Within the mixed layer, anisotropies seem to be negligible in comparison with the isotropic contributions. This is further confirmed by the test case, where results at 256^3 are compared with results at 512^3, without any significant discrepancy. We can conclude that the tendency to recover isotropy in the inertial range is not due to the subgrid-scale model or to finite size effects, but seems to be a genuine feature.

Injecting in the systems fluctuations with a different degree of convection does not seem to play a key role for the velocity and the temperature fields, whose lead-

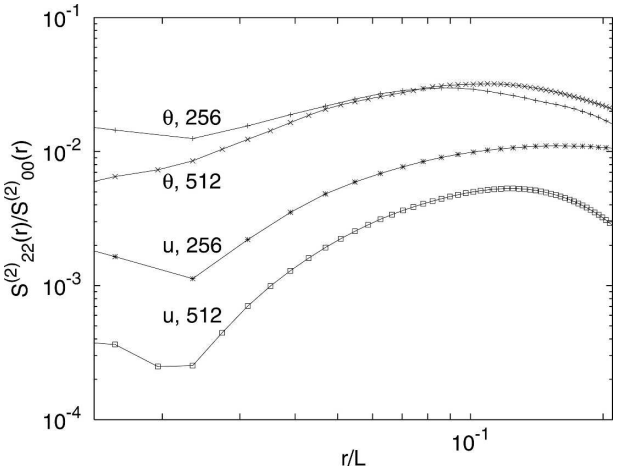

FIG. 19. Log–log plot of the ratio between an anisotropic projection to the isotropic one $S^{(2)}_{22}(r)/S^{(2)}_{00}(r)$, for the potential temperature and the velocity field, at varying the numerical resolution (see labels).

ing isotropic scaling exponents are only weakly or no dependent from the large-scale conditions, within the present error bars.

These results can give fruitful indications when studying the behavior of statistical observables within the mixed layer. From our results, it turns out that one can use the same set of (isotropic) scaling exponents to construct SGS multifractal parameterizations for atmospheric boundary layer flows having different degree of convection, since the dependence on large-scale features is weak.

Clearly, the relative weight of anisotropic terms, at the smallest scales (e.g., at those comparable to the filter size), becomes more and more negligible as the Reynolds number increases. However even using an LES with a spatial resolution smaller than the present one, the anisotropic projections give relatively small contributions compared to the isotropic terms. This is true for numerical resolutions larger than a minimum one, at which isotropic and anisotropic contributions can eventually reach the same order of magnitude. For the cases considered in this work, such critical resolution is quite small. It should be of the order of 64^3 grid points, if one accepts as a threshold, for example, on the second-order structure function, an anisotropic component with magnitude equal to the 5% of the isotropic counterpart. The critical resolution becomes smaller for lower thresholds.

A problem left open by our work is whether or not the conclusions drawn for convective boundary layers can be exported to the case of stably stratified boundary layers also (Andren 1995). In the latter situation, because of the presence of gravity waves, energy is transferred toward smaller scales via nonlinear wave–wave interactions. The final result of these interactions is that one passes from large-scale disturbances to disturbances at smaller scales, finally dissipated by SGS terms. The mechanism of energy transfer at work in wave–wave interactions is completely different from the energy cascade à la Kolmogorov. Both the universality picture and the isotropy restoration scenario could thus disappear in stably stratified boundary layers.

Another interesting issue to be explored is related to the possible anisotropy persistence close to the upper/bottom boundaries. There, scales of motion smaller than the LES filter size can be generated with the final result that turbulent fields are, at best, strongly sensitive to the particular subgrid scale model adopted. Today, only large Reynolds number experiments can possibly answer these questions.

Acknowledgments. This work has been supported by MIUR-Cofin 2005 Project 2005027808 and by CINFAI consortium. Simulations have been performed at the supercomputing center CINECA (Italy) in the framework of an INFM Parallel Computing Initiative. We particularly acknowledge Umberto Rizza for his help when performing high-resolution LES, and for sharing with us data and useful comments. We also thank Luca Biferale for useful discussions.

REFERENCES

Andren, A., 1995: The structure of stably stratified atmospheric boundary layers: A large-eddy simulation study. *Quart. J. Roy. Meteor. Soc.,* **121,** 961–985.

Antonelli, M., A. Mazzino, and U. Rizza, 2003: Statistics of temperature fluctuations in a buoyancy-dominated boundary layer flow simulated by a large eddy simulation model. *J. Atmos. Sci.,* **60,** 215–224.

Arad, I., V. L'vov, and I. Procaccia, 1999a: Correlations functions in isotropic and anisotropic turbulence: The role of the symmetry group. *Phys. Rev. E,* **59,** 6753–6788.

——, L. Biferale, I. Mazzitelli, and I. Procaccia, 1999b: Disentangling scaling properties in anisotropic and inhomogeneous turbulence. *Phys. Rev. Lett.,* **82,** 5040–5043.

——, ——, and I. Procaccia, 2000: Nonperturbative spectrum of anomalous scaling exponents in the anisotropic sectors of passively advected magnetic fields. *Phys. Rev. E,* **61,** 2654, doi:10.1103/PhysRevE.61.2654.

Basu, S., E. Foufoula-Georgiou, and F. Porté-Agel, 2004: Synthetic turbulence, fractal interpolation and large-eddy simulation. *Phys. Rev. E,* **70,** 026 310, doi:10.1103/PhysRevE.70.026310.

Biferale, L., and M. Vergassola, 2001: Isotropy vs anisotropy in small-scale turbulence. *Phys. Fluids,* **13,** 2139–2141.

——, and I. Procaccia, 2005: Anisotropy in turbulent flows and in turbulent transport. *Phys. Rep.,* **414,** 43–164.

——, I. Daumont, A. Lanotte, and F. Toschi, 2002: Anomalous and dimensional scaling in anisotropic turbulence. *Phys. Rev. E,* **66,** 056 306, doi:10.1103/PhysRevE.66.056306.

——, E. Calzavarini, F. Toschi, and R. Tripiccione, 2003: Universality of anisotropic fluctuations from numerical simulations of turbulent flows. *Europhys. Lett.,* **64,** 461–464.

Celani, A., A. Lanotte, A. Mazzino, and M. Vergassola, 2001: Fronts in passive scalar turbulence. *Phys. Fluids,* **13,** 1768–1783.

Deardorff, J. W., 1972: Numerical investigation of the planetary boundary layer with an inversion lid. *J. Atmos. Sci.,* **29,** 91–115.

Falkovich, G., K. Gawędzki, and M. Vergassola, 2001: Particles and fields in fluid turbulence. *Rev. Mod. Phys.,* **73,** 913–1069.

Frisch, U., 1995: *Turbulence: The Legacy of A. N. Kolmogorov.* Cambridge University Press, 296 pp.

Hofbauer, T., J. M. L. M. Palma, L. Biferale, and S. M. A. Gama, 2005: Anisotropy in large-eddy simulations determined from SO(3) symmetry group. *J. Turbul.,* **6,** 10.1080/14685240500125435.

Kolmogorov, A. N., 1941: Dissipation of energy in a locally isotropic turbulence. *J. Dokl. Akad. Nauk SSSR,* **32,** 16–18.

Kraichnan, R. H., 1994: Anomalous scaling of a randomly advected passive scalar. *Phys. Rev. Lett.,* **72,** 1016–1019.

Kurien, S., V. L'vov, I. Procaccia, and K. R. Sreenivasan, 2000: Scaling structure of the velocity statistics in atmospheric boundary layers. *Phys. Rev. E,* **61,** 407–421.

——, K. G. Aivalis, and K. R. Sreenivasan, 2001: Anisotropy of small-scale scalar turbulence. *J. Fluid Mech.,* **448,** 279–288.

Lanotte, A., and A. Mazzino, 1999: Anisotropic non-perturbative zero modes for passively advected magnetic fields. *Phys. Rev. E,* **60,** R3483, doi:10.1103/PhysRevE.60.R3483.

Mason, P. J., 1994: Large-eddy simulation: A critical review of the technique. *Quart. J. Roy. Meteor. Soc.,* **120,** 1–26.

Meneveau, C., and J. Katz, 2000: Scale-invariance and turbulence models for large-eddy simulation. *Annu. Rev. Fluid Mech.,* **32,** 1–32.

Minnini, P. D., A. Alexakis, and A. Pouquet, 2006: Large-scale flow effects, energy transfer, and self-similarity on turbulence. *Phys. Rev. E,* **74,** 16 303, doi:10.1103/PhysRevE.74.016303.

Moeng, C.-H., 1984: A large-eddy-simulation model for the study of planetary boundary-layer turbulence. *J. Atmos. Sci.,* **41,** 2052–2062.

——, and P. P. Sullivan, 1994: A comparison of shear- and buoyancy-driven planetary boundary layer flows. *J. Atmos. Sci.,* **51,** 999–1021.

Nieuwstad, F. T. M., and R. A. Brost, 1986: The decay of convective turbulence. *J. Atmos. Sci.,* **43,** 532–546.

Pumir, A., and B. Shraiman, 1995: Persistent small scale anisotropy in homogeneous shear flows. *Phys. Rev. Lett.,* **75,** 3114–3117.

Scotti, A., and C. Meneveau, 1997: Fractal model for coarse-grained partial differential equations. *Phys. Rev. Lett.,* **78,** 867–870.

Shen, X., and Z. Warhaft, 2000: The anisotropy of the small scale structure in high Reynolds number (R_λ 1000) turbulent shear flow. *Phys. Fluids,* **12,** 2976–2989.

Shraiman, B. I., and E. D. Siggia, 2000: Scalar turbulence. *Nature,* **405,** 639–646.

Spalart, P., R. Moser, and M. Rogers, 1991: Spectral methods for the Navier-Stokes equations with one infinite and two periodic directions. *J. Comput. Phys.,* **96,** 297–324.

Sreenivasan, K. R., and R. A. Antonia, 1997: The phenomenology of small-scale turbulence. *Annu. Rev. Fluid Mech.,* **29,** 435–472.

Sullivan, P. P., J. C. McWilliams, and C.-H. Moeng, 1994: A subgrid-scale model for large-eddy simulation of planetary boundary layer flows. *Bound.-Layer Meteor.,* **71,** 247–276.

Warhaft, Z., 2000: Passive scalars in turbulent flows. *Annu. Rev. Fluid Mech.,* **32,** 203–240.